13.4   An Assessment of Buoyancy and Baroclinity within Select VORTEX2 Storms

Christopher C. Weiss[*]
Texas Tech University, Lubbock, Texas

David C. Dowell
NOAA/ESRL, Boulder, Colorado

Patrick S. Skinner, Anthony E. Reinhart
Texas Tech University, Lubbock, Texas

1. INTRODUCTION

Numerical and observational studies have suggested a number of processes relevant to the generation, reorientation and amplification of vorticity within supercell thunderstorms. Baroclinic horizontal vorticity generation related to gradients of buoyancy is one area that has received considerable attention over the past couple of decades (e.g., Rotunno and Klemp 1985; Davies-Jones and Brooks 1993; Adlerman et al. 1999; Davies-Jones 2000; Markowski et al. 2012a,b). Though a few field projects have provided opportunities for in situ sampling of surface conditions within these storms, mostly using various versions of mobile mesonet platforms (Straka et al. 1996), up until the Verification of the Origin of Rotation in Tornadoes Experiment 2 (VORTEX2) there had yet to be a concentrated effort to map thermodynamic fields at the surface over the entire storm scale. Ultimately, the charge is to better discriminate the characteristic buoyancy (and gradients thereof) across the spectrum of VORTEX2 storms, and relate these variations to observed differences in tornado production.

During the 2009 and 2010 field phases of VORTEX2, approximately 650 StickNet probes were deployed in total. Details of the StickNet instruments and an overview of the deployments can be found in Weiss et al. (2010).

2. ANALYSIS METHODOLOGY

All StickNet data from VORTEX2 were first quality controlled to account for unrealistic values (e.g., in time periods where the instrumentation was known to be damaged). The data used for analysis were then debiased according to the

* Corresponding author address: Christopher C. Weiss, Texas Tech University, Atmospheric Science Group, Department of Geosciences, Lubbock, TX, 79409; e-mail: Chris.Weiss@ttu.edu

results of mass probe tests, which sporadically occurred through the field phase on inactive days.

Data were then subjected to a standard time-to-space conversion using a constant storm motion, which in these two cases was estimated using the motion of specific radar reflectivity features and, additionally in the case of Seminole, OK, tornado vortex translation. As all time-to-space analyses are centered at the time when the strongest inferred vertical vorticity (from single Doppler radar coverage in both cases) crossed the StickNet array, errors in the storm motion (and the inherent assumption of supercell stationarity) accrue as one heads outwards from the center of the domain in both directions. That said, comparisons of radar radial velocity with StickNet winds suggest these errors are not terribly significant, even at times +/- 30 min from the center of the analysis.

A two-pass Barnes objective analysis was performed on time-to-space converted data, the results of which are presented in this paper. Following the suggestions of previous studies, a convergence parameter of $\gamma=0.1$ and a smoothing parameter of $\kappa=(1.33\ \Delta y)^2$ were used (Pauley and Wu 1990), where Δy represents a typical along-deployment line station spacing. Mobile radar data from the Doppler on Wheels (DOW), Shared Mobile Atmospheric Research and Training Radars (SMART-R), and the MWR-05XP Mobile Phased Array Weather Radar were similarly subjected to a separate Barnes filter. The coordinate origin of all presented analyses was set to the objectively determined maximum in azimuthal shear of radial velocity, using an algorithm that integrated this shear over a 1 to 10 km width.

Thermodynamic variables in this study are calculated similarly to those in previous studies. Virtual potential temperature is used in place of density potential temperature owing to the fact that radar reflectivity information, used in the estimate of liquid water mixing ratio, was either too coarse (e.g., WSR-88D) or uncalibrated (e.g., DOW).

Equivalent potential temperature is defined as by Bolton (1980).

The definition of the base state is rather subjective and varies across studies. We choose to define the base state at a position just outside the edge of the forward anvil from the target storm. As such, points in the near-field inflow of target storms will generally show thermodynamic deficits relative to this chosen base state. In both of the cases presented here, the base state is calculated from a surface observation exactly two hours ahead of the updraft passage.

3. 18 MAY 2010 CASE – DUMAS, TX

Overview

On 18 May 2010, VORTEX2 teams intercepted a long-lived supercell thunderstorm that traversed from west of Dumas, TX past Stinnett, TX. According to the log maintained by the Storm Prediction Center, seven (weak) tornadoes were reported, stretching from Dumas westward about 40 km (Fig. 1).

Two north-south arrays of StickNet probes were deployed, the first along US-287 north/south from Dumas, the second north/south along FM-1060 at a longitude ~30 km east of Dumas (Fig. 1). Each array consisted of 12 probes extending over a ~30-40 km swath, with finer station spacing near the location of the low-level mesocyclone. The first array received the updraft portion of the storm near the time of two weak tornadoes (~2330 UTC), then the target storm entered a largely non-tornadic phase for the following 55 minutes leading up to passage through the second StickNet array (~0025 UTC). Radar observations from the DOW and MWR_05XP (not shown) confirm that the azimuthal shear of radial velocity is indeed much weaker at the time of the second StickNet intercept. Inferred vertical vorticity, (assuming the structure of a Rankine vortex as in Markowski et al. 2012a) is one magnitude larger ($O\sim(10^{-1}\ s^{-1})$) during the first StickNet deployment. Considering these pieces of evidence, we choose to identify StickNet deployment #1 (hereafter, D1) as "weakly tornadic" and deployment #2 (hereafter, D2) as "non-tornadic", a distinction that will be used when interpreting the results.

A salient feature of this storm was the volume and size of hail produced. These hailstones damaged the anemometry of two probes dropped in deployment #2. Further, a shallow hail fog was noticed during the retrieval of probes, suggesting the coverage was significant enough to have a thermodynamic footprint.

Results

The kinematic presentations for both StickNet deployments (Figs. 2a,b) have many similarities. The inflow environment is consistently defined by a southeasterly ~20 kt wind. Rear-flank downdraft air is clearly visible in the expected areas flanking and wrapping around the low-level mesocyclone (at 0,0).

One rather noticeable difference between the two deployments is the character of winds near the forward-flank reflectivity gradient (FFRG). Ground-relative winds are much more northerly in D1 than D2, the latter of which features a less-obvious axis of confluence (Fig. 2b). It is acknowledged that the FFRG-relative probe position is somewhat different for the two cases, but overlap does exist, and the differing sense of the winds is confirmed by multiple rows of probes. The more backed winds in D1 within the FFRG are broadly consistent with the traditional concept of a forward-flank downdraft / gust front (e.g., Lemon and Doswell 1979).

The thermodynamic depiction of D1 and D2 also show some similarities. Equivalent potential temperature deficits are rather significant, exceeding 16 ^{o}C (11 ^{o}C) at positions well rearward and to the left of the low-level mesocyclone (Figs. 3a,b). At the center of the low-level mesocyclone, deficits are more modest, near 4 ^{o}C (6 ^{o}C) for D1 (D2), though rather sharp gradients exist in both cases. A noted weakness in θ_e deficits is evident along the FFRG for the D2 deployment, similar to a feature noted by Skinner et al. (2011) for a supercell case near Perryton, TX on 23 May 2007. The fact that just one probe was in proper position to capture this signal is cause for some concern. However, this probe showed no bias in a mass test carried out the previous day, nor was a bias evident at the time of deployment, in comparison to surrounding StickNet obs.

Virtual potential temperature gradients within the FFRG are to some degree influenced by the positioning of probes for the two deployments. That notwithstanding, the magnitude of θ_v gradients does overall appear to be stronger in the case of D1 across the FFRG (Figs. 4a,b), consistent with the more backed ground-relative winds mentioned earlier, and near the low-level mesocyclone.

The signature of hail fall is quite apparent as "tracks" in the deficit fields for the two probes affected in D2. Deficits in θ_e (θ_v) are increased roughly 3 K (2 K) locally in these areas.

4. 10 MAY 2010 CASE – SEMINOLE, OK

Overview

The 10 May 2010 case in east-central Oklahoma represents a sharp contrast to the previous case. A widespread outbreak of rapidly moving tornadic supercells occurred, the widest of which (determined from the NWSFO Norman, OK survey) traveled from near Tecumesh, OK to Cromwell, OK (Fig. 5).

Though the rapid storm motion prohibited coordinated VORTEX2 sampling, the StickNet teams were able to deploy a single line of ten probes along US-377 north from Seminole, OK (Fig. 5). The southern portion of this array was impacted by the tornado near where the path was rated EF3. Though probes were deployed with considerably less lead time than in the Dumas, TX case, a sufficient sample of the forward precipitation region and FFRG was achieved for comparison.

Results

The kinematic depiction of this case (Fig. 6) is rather similar to D1 (cf. Fig. 2) in that a clear northerly component ground-relative wind was present near the FFRG, consistent with a clear east-west axis of confluence. Considering the sea-level pressure field from the same time (Fig. 7), we see that these winds are consistent with a northward-directed pressure gradient, partly driven by an increase of pressure within the precipitation core (again, akin to the traditional conceptual model of a forward-flank downdraft) and pressure falls within the inflow environment, ahead of where the rear-flank gust front (RFGF) intersects the FFRG.

Thermodynamic deficits are overall weaker than those exhibited for the Dumas case, particularly D1. Maximum deficits in θ_e (θ_v) are approximately 11 K (5 K), again well to the rear and to the left of the low-mesocyclone/tornado (Figs. 8, 9). Equivalent potential temperature deficit near the tornado itself is only about 3 K. Gradients of θ_v are much weaker near the low-level vertical vorticity maximum compared to the D1 and D2 analyses, and somewhat perpendicular to the FFRG.

One particularly unusual feature is the rapid increase in θ_e behind the low-level mesocyclone/tornado (Fig. 8). In fact, relative to the base state, equivalent potential temperature actually shows a significant *surplus* upwards of 7-8 K in this region. This increase in equivalent

potential temperature is tied almost entirely to dewpoint, which increases to near 23 °C over the two probes (0103A, 0105A) measuring this feature. Liquid water intrusion into the housing for the temp/RH sensor is being considered as an explanation as both probes were subject to high winds > 30 m s^{-1} during the deployment. However, neither of the probes shows RH > 96% at any point. Further, probe 0111A shows a similar trend in water vapor with weaker winds.

5. COMPOSITE ANALYSES

Objective analyses from the three StickNet deployments (D1, D2, Seminole) were composited and differenced to compare the storm-scale thermodynamic structure. Composites of θ_e and θ_v (Figs. 10a, 10b) reveal the strongest deficits in the areas expected, to the left and rear of the low-level mesocyclone. On average, these maximum deficits were located approximately 10 km to the north and west of the low-level mesocyclone. Rather sharp gradients in θ_e exist along the reflectivity gradient behind the low-level mesocyclone. A trough in the thermodynamic perturbations appears to run near the highest radar reflectivity in the forward flank. Deficits in θ_v show a monotonic increase as one moves counter-clockwise from the inflow environment through the precipitation core. However, the gradients do seem somewhat bifurcated in these composites, with stronger gradients located near the FFRG and farther back towards the rear of the precipitation core. These gradients are all of proper sign to allow for the generation of streamwise-component horizontal vorticity for typical trajectories entering the low-level mesocyclone (e.g., Klemp and Rotunno 1985; Wicker and Wilhelmson 1995; Markowski 2002b; Beck and Weiss 2013).

The differencing of D1 (weakly tornadic) and D2 (non-tornadic) (Fig. 11) reveals a stronger gradient of θ_v across the FFRG in the case of D1, although interpretation is somewhat muddled by the different probe positioning between the two deployments. However, a similar indication is present when differencing Seminole (tornadic) and D2 (non-tornadic), though more towards the far field (e.g., 12,6). (In both cases, the gradient of the difference field aligns with the gradient of θ_v, leading to this result).

6. SUMMARY AND CONCLUSIONS

Three VORTEX2 cases are chosen for analysis in this study, with a focus on how storm-scale thermodynamics vary. The three deployments represent a spectrum of tornado production, where the Dumas deployments D1 (D2) are weakly (non-) tornadic, and the third case from Seminole represents a strongly tornadic storm.

The following conclusions are put forth from this research:

- The strongly tornadic Seminole, OK case featured much weaker thermodynamic deficits, in line with previous investigations (e.g., Markowski et al. 2002),
- Composite depictions of virtual potential temperature reveal a somewhat bifurcated nature to these gradients, suggesting there are separate zones for enhanced baroclinic generation of horizontal vorticity, one near the FFRG, the other more towards the rear portion of the precipitation core,
- Gradients of θ_v along the FFRG tend to be stronger in the tornadic cases,
- Clear axes of confluence, akin to the traditional depiction of forward-flank gust fronts, are apparent near the FFRG in tornadic cases, supported in part by measured northward gradients in MSLP,
- Surpluses in θ_e have been shown to exist in the wake of the Seminole, OK storm, and
- Hail fall has a thermodynamic footprint within the forward flank of the Dumas storm.

7. ACKNOWLEDGEMENTS

8. REFERENCES

Adlerman, E. J., K. K. Droegemeier, and R. Davies-Jones, 1999: A numerical simulation of cyclic mesocyclogenesis, *J. Atmos. Sci.,* **56**, 2045-2069.

Beck, J. R., and C. C. Weiss, 2013: An assessment of low-level baroclinity and vorticity within a simulated supercell. *Mon. Wea. Rev.*, (in press).

Bolton, D., 1980: The computation of equivalent potential temperature. *Mon. Wea. Rev.*, **108**, 1046-1053.

Davies-Jones, R. P., 2000: A Lagrangian model for baroclinic genesis of mesoscale vortices. Part I: Theory. *J. Atmos. Sci.*, **57**, 715-736.

Davies-Jones, R. P., and H. E. Brooks, 1993: Mesocyclogenesis from a theoretical perspective. *The Tornado: Its Structure, Dynamics, Prediction, ad Hazards. Geophys. Monogr.*, Vol. 79, Amer. Geophys. Union, 105-114.

Lemon, L. R., and C. A. Doswell III, 1979: Severe thunderstorm evolution and mesocyclone structure as related to tornadogenesis. *Mon. Wea. Rev.*, **107**, 1184-1197.

Markowski, P. M., J. M. Straka, and E. N. Rasmussen, 2002: Direct surface thermodynamic observations within the rear-flank downdrafts of nontornadic and tornadic supercells, *Mon. Wea. Rev.*, **130**, 1692-1721.

Markowski, P. M., Y. Richardson, J. Marquis, R. Davies-Jones, J. Wurman, K. Kosiba, P. Robinson, E. Rasmussen, D. Dowell, 2012a: The pretornadic phase of the Goshen County, Wyoming, supercell of 5 June 2009 intercepted by VORTE2. Part I: Evolution of kinematic and surface thermodynamic fields. *Mon. Wea. Rev.*, **140**, 2887-2915.

Markowski, P. M., Y. Richardson, J. Marquis, R. Davies-Jones, J. Wurman, K. Kosiba, P. Robinson, E. Rasmussen, D. Dowell, 2012b: The pretornadic phase of the Goshen County, Wyoming, supercell of 5 June 2009 intercepted by VORTE2. Part II: Intensification of low-level rotation. *Mon. Wea. Rev.*, **140**, 2916-2938.

Pauley, P. M., and X. Wu, 1990: The theoretical, discrete, and actual response of the Barnes objective analysis scheme for one- and two-dimensional fields. *Mon. Wea. Rev.,* **118**, 1145-1164.

Rotunno, R. and J. Klemp, 1985: On the rotation and propagation of simulated supercell thunderstorms. *J. Atmos. Sci.*, **42**, 271-292.

Skinner, P. S., C. C. Weiss, J. L. Schroeder, L. J. Wicker, and M. I. Biggerstaff, 2011: Observations of the surface boundary structure within the 23 May 2007 Perryton, Texas supercell. *Mon. Wea. Rev.*, **139**, 3730-3749.

Straka, J. M., E. N. Rasmussen, S. E. Fredickson, 1996: A mobile mesonet for finescale meteorological observations. *J. Atmos. Oceanic Technol.*, **13**, 921-936.

Wicker, L. J., and R. B. Wilhelmson, 1995: Simulation and analysis of tornado development and decay within a three-dimensional supercell thunderstorm. *J. Atmos. Sci.*, **52**, 2675-2703.

Weiss, C. C. and D. Dowell, 2010: Highlights from the Texas Tech Ka-band mobile Doppler radar and StickNet data collection during VORTEX2. *Preprint, 25th Conf. on Sev. Local Storms*, Denver, CO, paper 5.5.
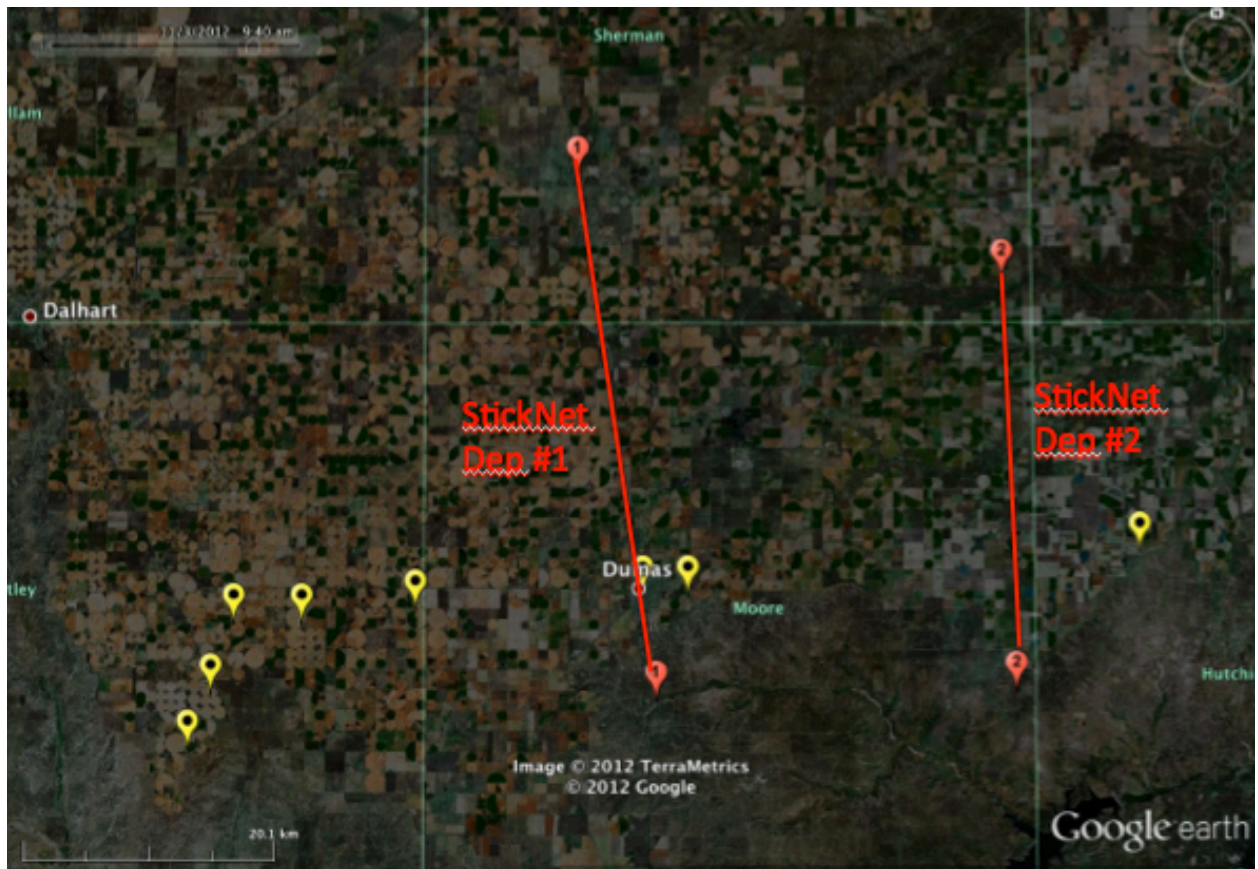
Figure 1 – An overview of the two StickNet deployments from 18 May 2010. Dumas, TX is indicated. Yellow markers represent the location of tornado reports from the Storm Prediction Center log.
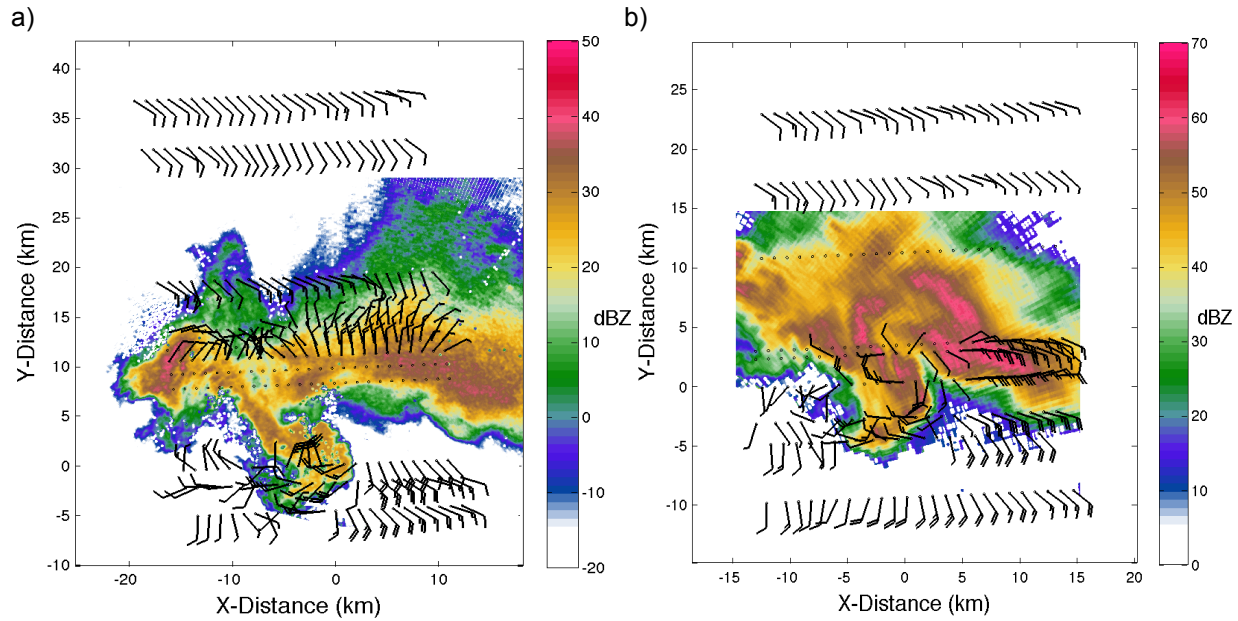
Figure 2 – Time-to-space converted StickNet data for a) deployment "D1" (2305-2355 UTC) and b) deployment "D2" (0000-0050 UTC) overlaid with (shaded) mobile radar reflectivity from a) DOW6 (2.0 deg) at 2330 UTC and b) SMART-R1 (2.5 deg) at 0025 UTC. Distance scale is indicated on the axes. Winds are presented in kts (full barb = 10 kts, half barb = 5 kts) and are ground relative.
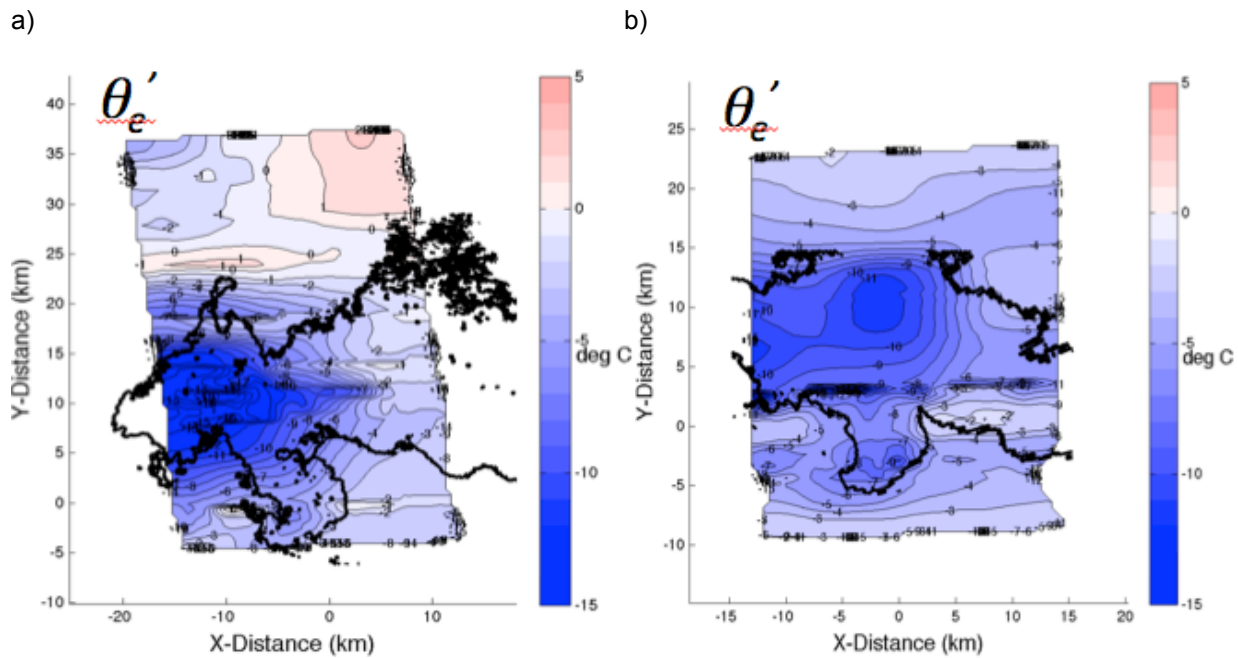
Figure 3 – (shaded) Time-to-space converted StickNet-derived equivalent potential temperature (deg C) for a) deployment "D1" (2305-2355 UTC) and b) deployment "D2" (0000-0050 UTC) overlaid with the a) 0 dBZe DOW6 (2.0 deg) reflectivity contour at 2330 UTC and b) 30 dBZ SMART-R1 (2.5 deg) reflectivity contour at 0025 UTC. Distance scale is indicated on the axes.
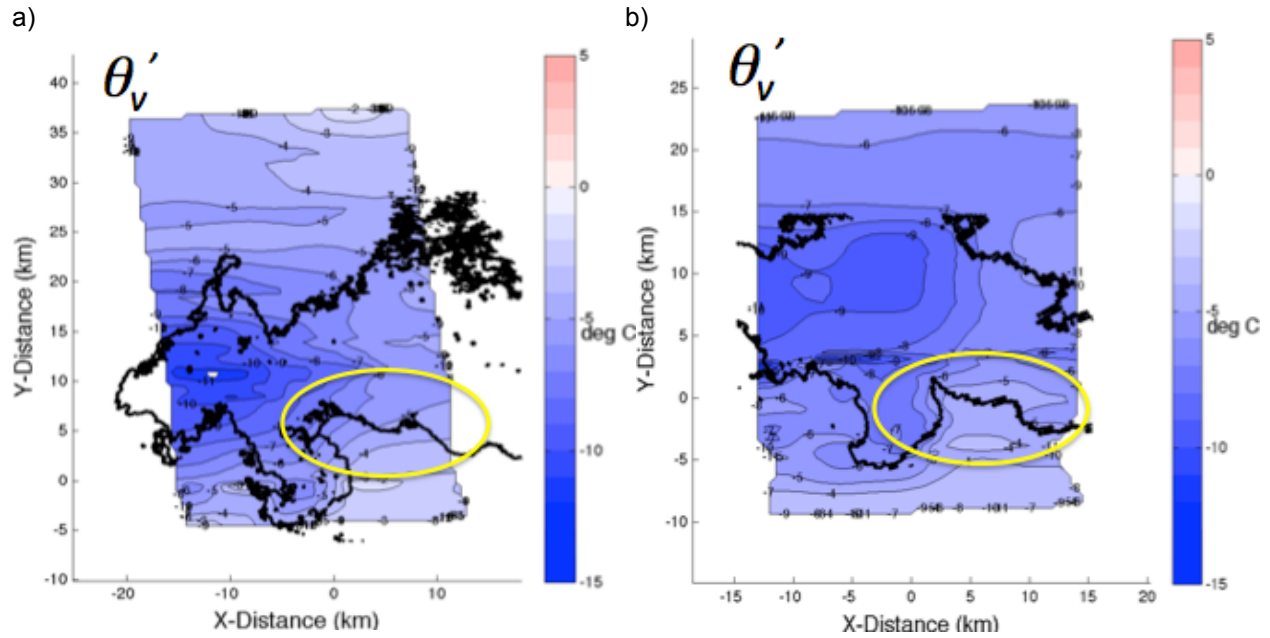
Figure 4 – as in Fig. 3, but for (shaded) virtual potential temperature (deg C). Yellow oval denotes location of FFRG that is discussed in the text.
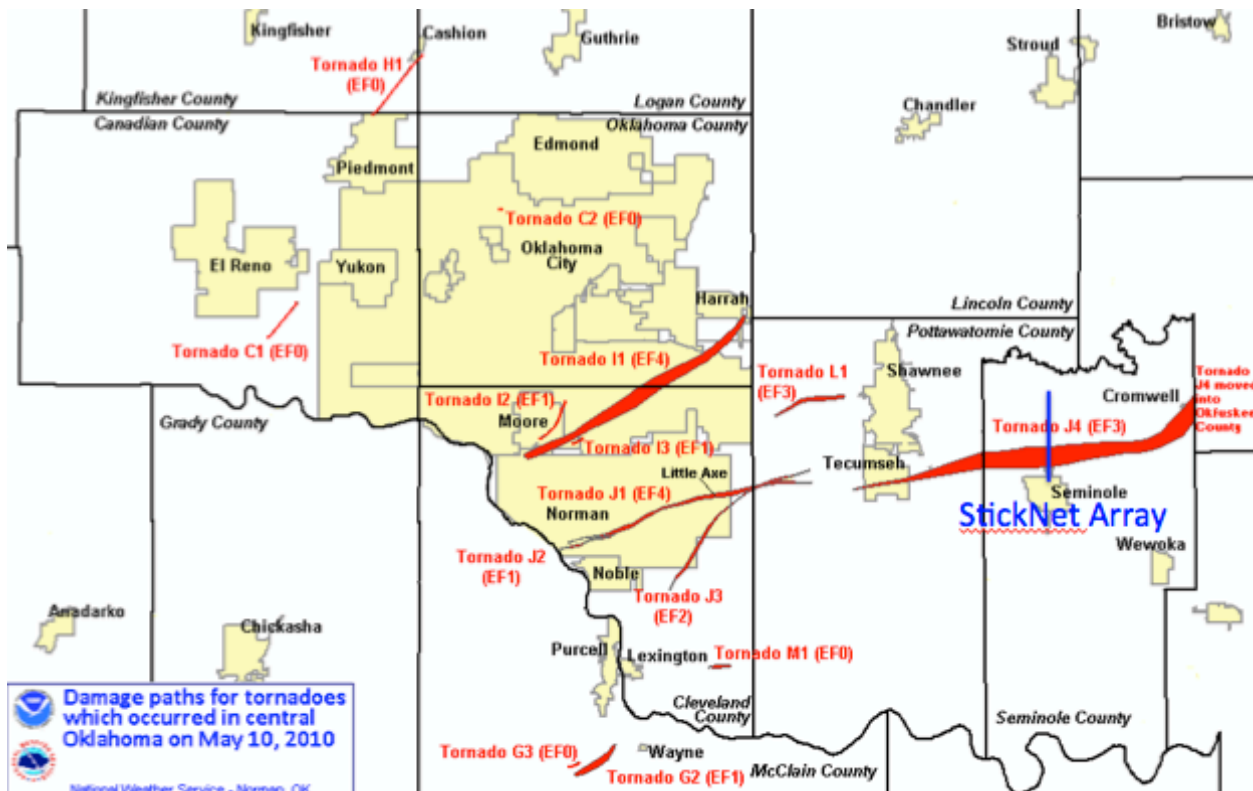
Figure 5 – Tornado damage paths determined by the National Weather Service Forecast Office – Norman, OK for the 10 May 2010 supercell outbreak in central and eastern Oklahoma. The blue line denotes the location of the StickNet array.
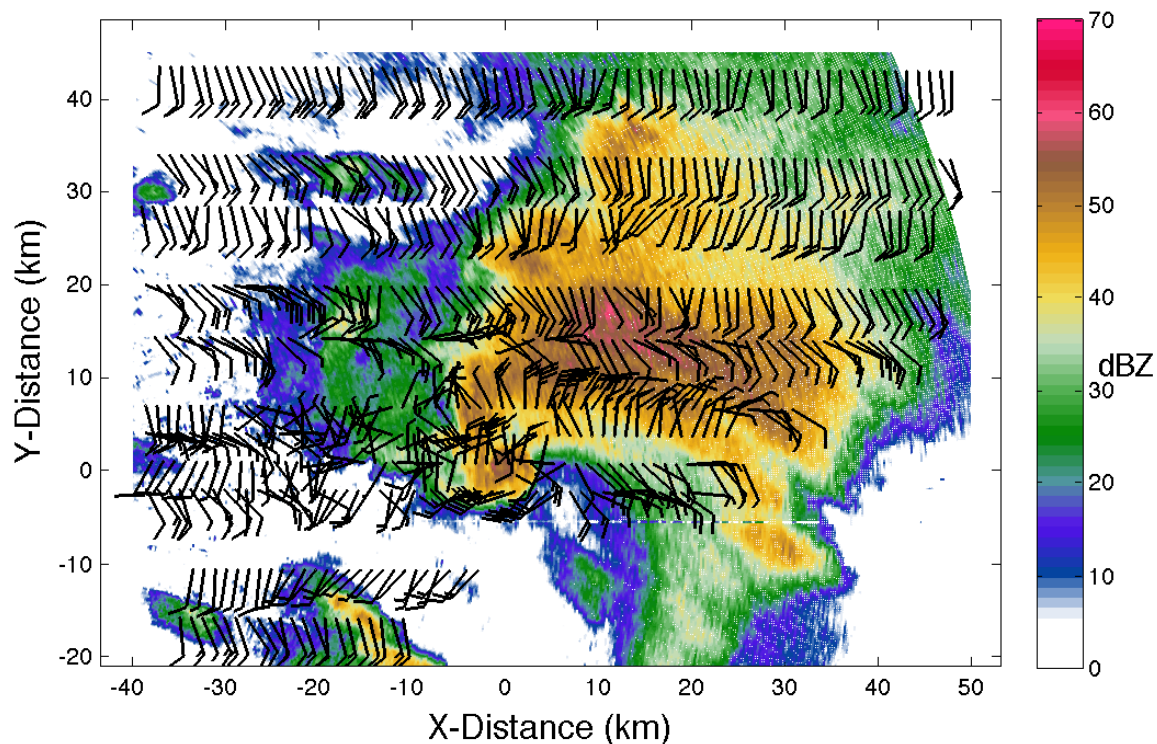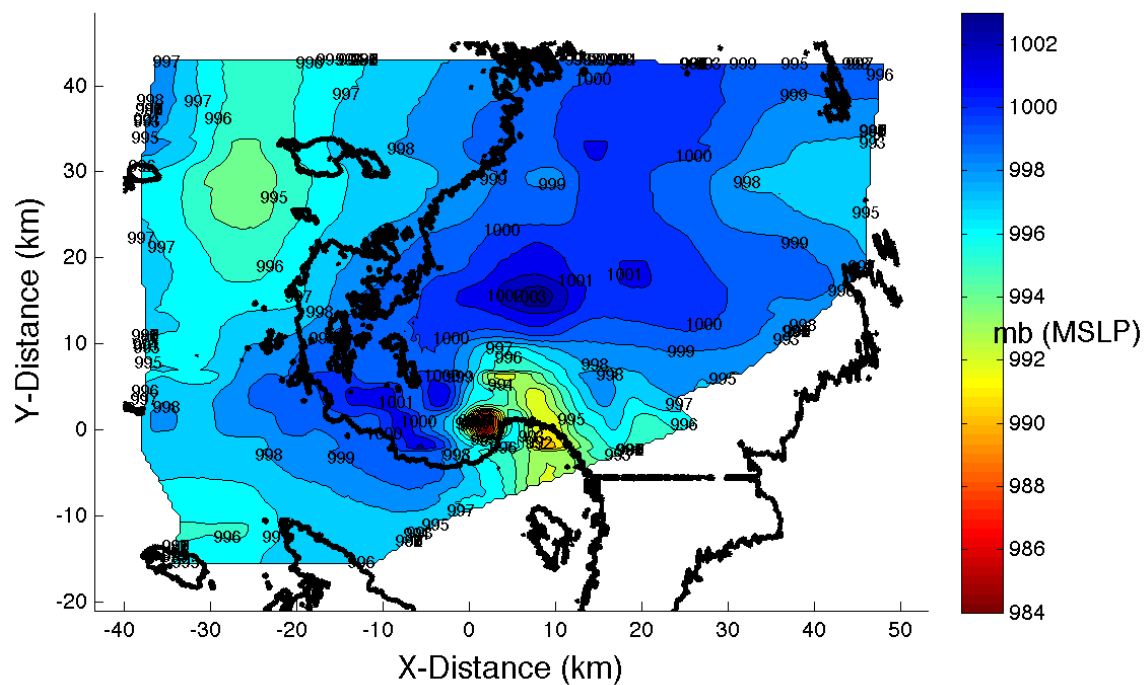
Figure 6 - Time-to-space converted StickNet data for the Seminole, OK deployment on 10 May 2010, 2248-2348 UTC, (shaded) KOUN 0.5 deg reflectivity at 2316 UTC. Distance scale is indicated on the axes. Winds are presented in kts (full barb = 10 kts, half barb = 5 kts) and are ground relative.

Figure 7 - (shaded) Time-to-space converted StickNet-derived MSLP (mb) for the Seminole, OK deployment on 10 May 2010, 2248-2348 UTC, overlaid with the 20 dBZ KOUN (0.5 deg) reflectivity contour at 2316 UTC. Distance scale is indicated on the axes.
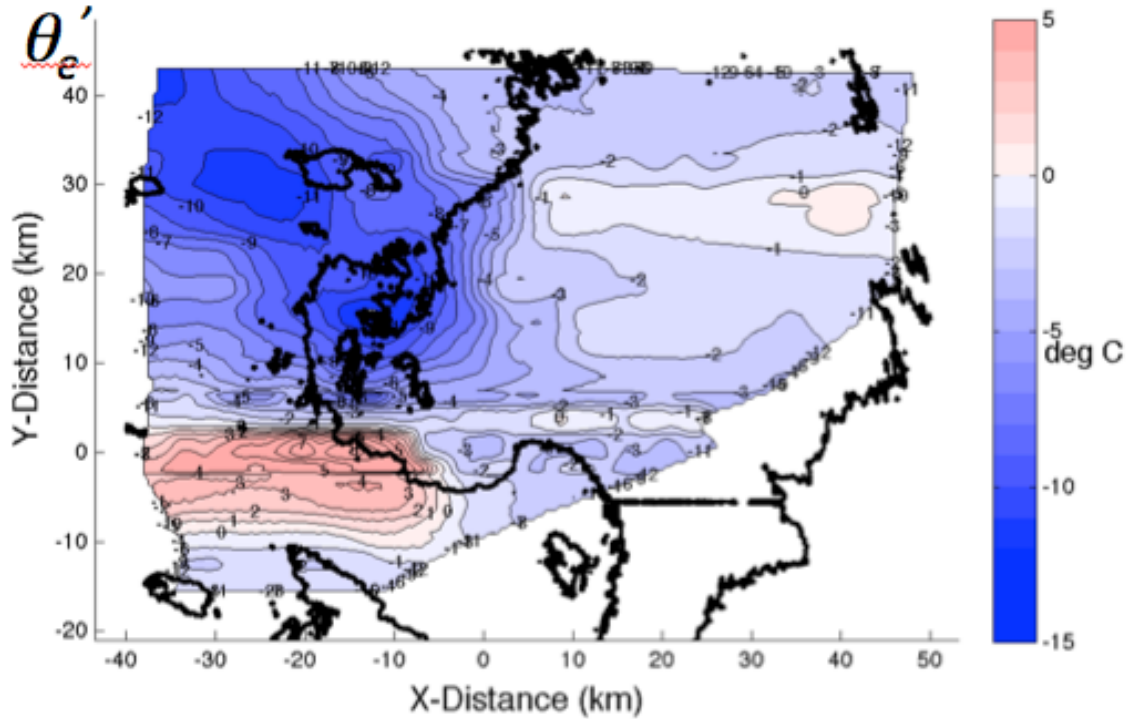
Figure 8 - (shaded) Time-to-space converted StickNet-derived equivalent potential temperature (deg C) for the Seminole, OK deployment on 10 May 2010, 2248-2348 UTC, overlaid with the 20 dBZ KOUN (0.5 deg) reflectivity contour at 2316 UTC. Distance scale is indicated on the axes.
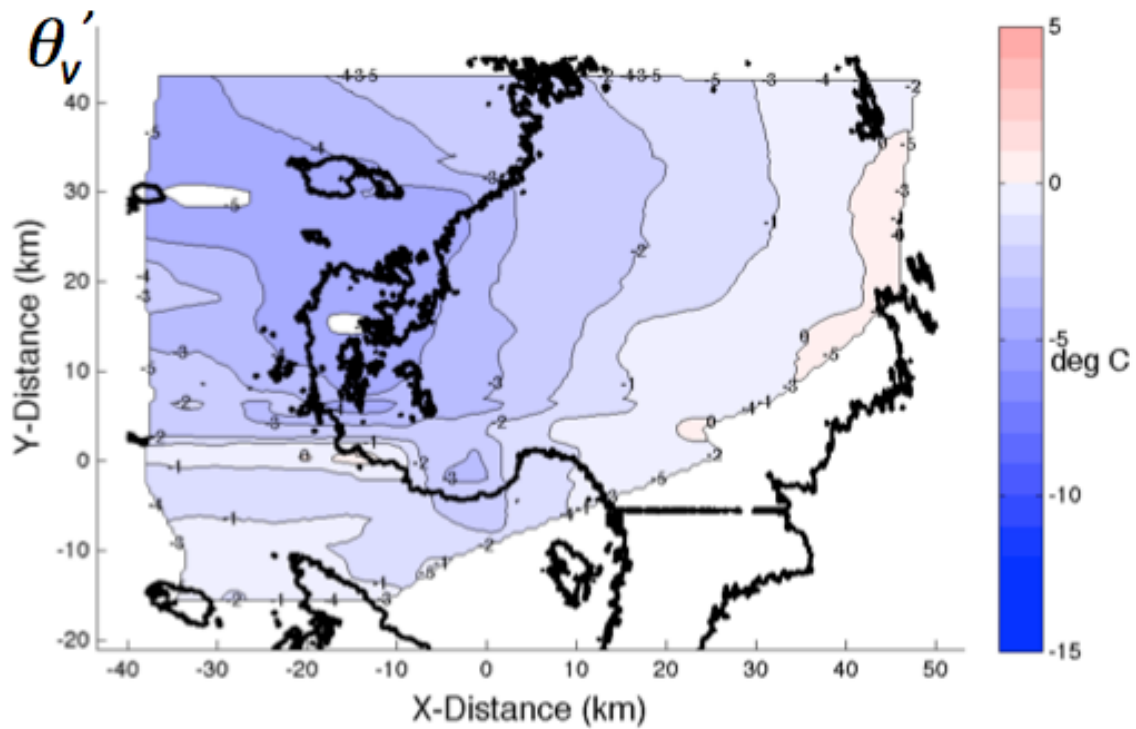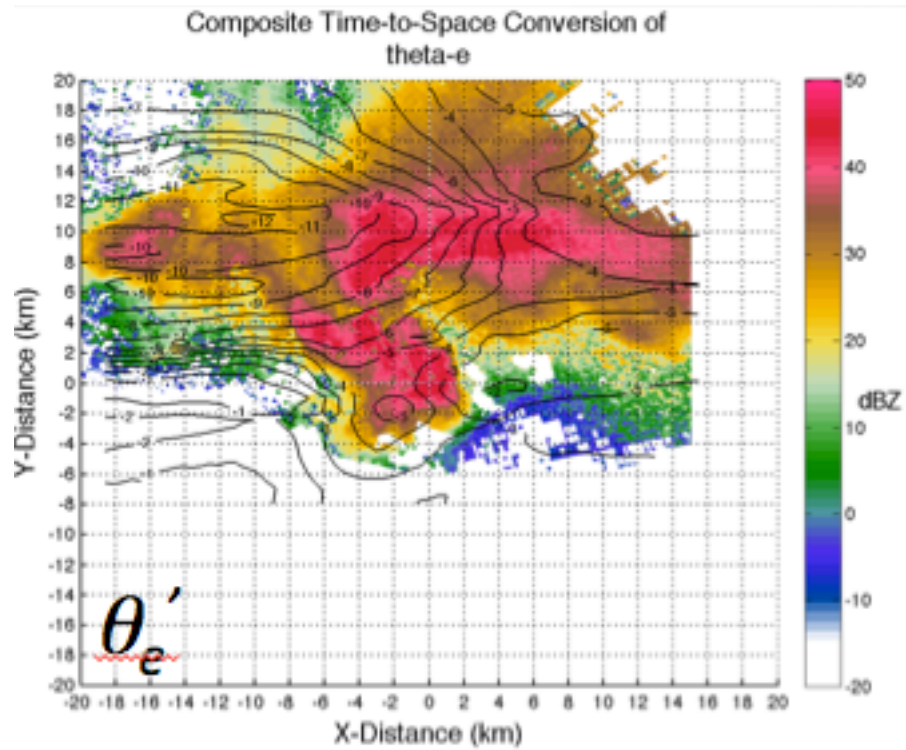

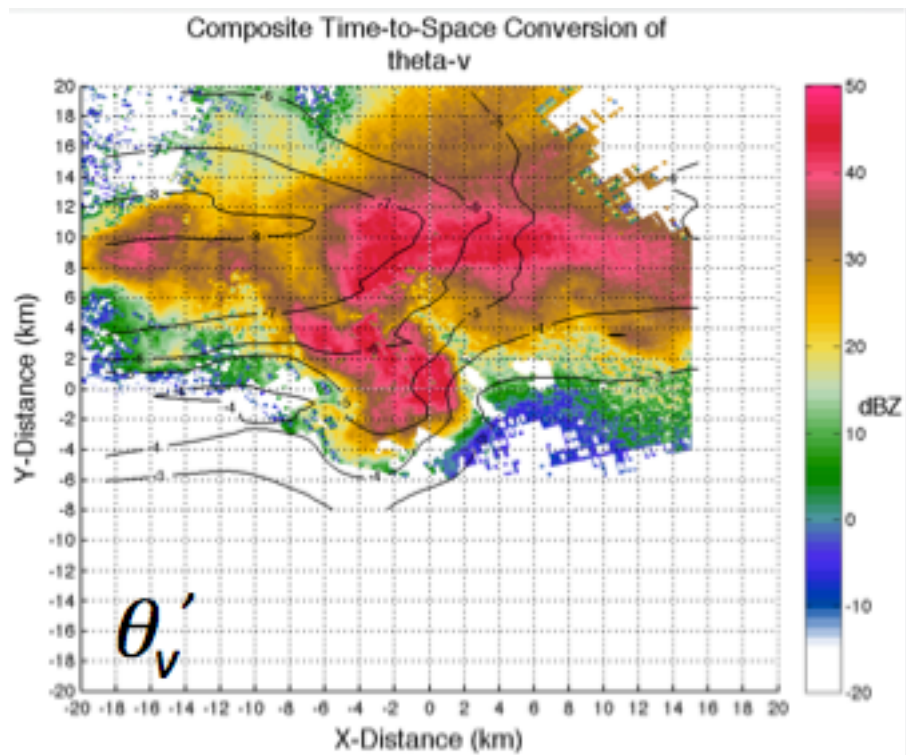Figure 9 – As in Fig. 8, but for (shaded) virtual potential temperature.
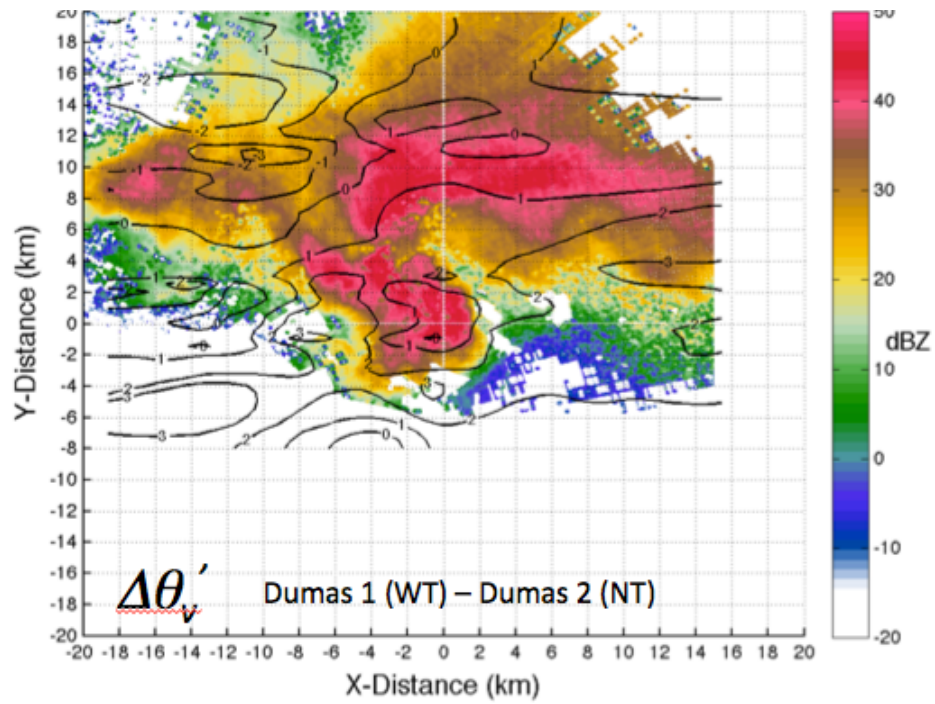
a)

b)

Figure 10 – Composite depictions of a) equivalent potential temperature and b) virtual potential temperature, contoured every 1 deg C, (shaded) composite radar reflectivity.
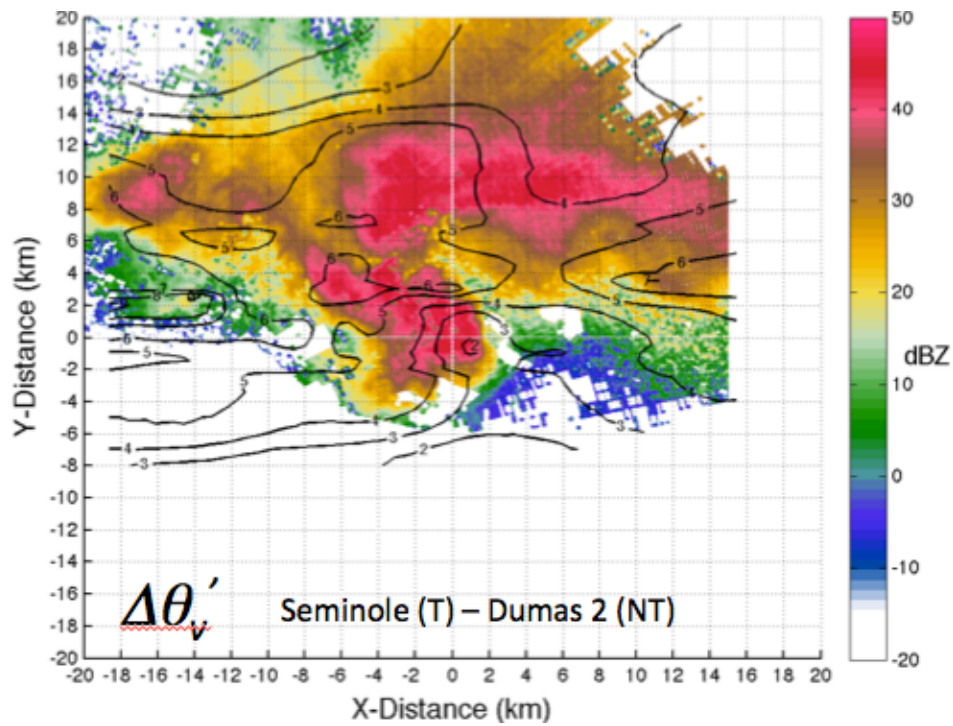
a)

b)

Figure 11 – Composite differences of virtual temperature for a) D1-D2 and b) Seminole – D2, contoured every 1 deg C, (shaded) composite radar reflectivity.